ScieRxiv

NOT PEER-REVIEWED

Research Article

Thermal exposure rewrites failure rules in SLM Al-Si-Fe-Mn-Ni lattices

Guangmeng Yang[1], Dabiao Xia[4], Ziting Chen[5], Jiaming Feng[1], Sinan Xiao[6], Heyuan Huang[3]*, Ben Jia[2]*

[1]Jihua Laboratory, Foshan 528200, Guangdong, China.

[2]Institute of Nuclear and New Energy Technology, Tsinghua University, Beijing 100084, China.

[3]School of Aeronautics, Northwestern Polytechnical University, Xi'an 710072, Shaanxi, China.

[4]Key Laboratory of Functional Materials and Devices for Informatics of Anhui Educational Institutions, Fuyang Normal University, Fuyang 236037, Anhui, China.

[5]School of Engineering, Guangdong Technion-Israel Institute of Technology, Shantou 515041, Guangdong, China.

[6]Shien-Ming Wu School of Intelligent Engineering, South China University of Technology, Guangzhou 511442, Guangdong, China.

Correspondence to: Prof. Heyuan Huang, School of Aeronautics, Northwestern Polytechnical University, Xi'an 710072, Shaanxi, China. E-mail: huangheyuan@nwpu.edu.cn; Dr. Ben Jia, Institute of Nuclear and New Energy Technology, Tsinghua University, Beijing 100084, China. E-mail: jiaben@mail.nwpu.edu.cn

Received: 06 May 2026 | Approved: 18 May 2026 | Online: 18 May 2026

Abstract

SLM-fabricated Al-Si-Fe-Mn-Ni alloy lattice structures offer attractive opportunities

© The Author(s) 2026 Open Access This article is licensed under a Creative Commons Attribution 4.0 International License (https://creativecommons.org/licenses/by/4.0/), which permits unrestricted use, sharing, adaptation, distribution and reproduction in any medium or format, for any purpose, even commercially, as long as you give appropriate credit to the original author(s) and the source, provide a link to the Creative Commons license, and indicate if changes were made.

for lightweight components operating under thermal loads, yet their topology-dependent thermal stability remains insufficiently understood. Here, we systematically examine two lattice configurations exposed at 200 °C and 300 °C for up to 500 h using mechanical testing, finite element simulation, TEM and EBSD. Both lattices retained excellent stability at 200 °C, whereas exposure at 300 °C caused gradual mechanical degradation and shifted the dominant failure mode from brittle fracture to buckling instability. Mechanical tests and simulations further revealed a strong dependence on lattice configuration. The topology with a higher second moment of area showed greater resistance to property degradation than the cross-core-supported design during prolonged exposure. Microstructural analysis showed that solute atoms progressively segregated to grain boundaries, forming a continuous second-phase network. This network generated a pronounced Zener pinning effect, suppressing grain coarsening and preserving the initial crystallographic texture. These findings clarify the mechanisms governing the thermal stability of this alloy system and provide a theoretical basis for designing thermally robust lattice components.

Keywords: Selective laser melting, lattice structure, heat-resistant aluminum alloy, thermal stability, failure mode transition

INTRODUCTION

Lightweight load-bearing components used in aerospace thermal protection systems must combine low density, structural stiffness and resistance to long-term thermal exposure[1-4]. Additively manufactured (AM) lattice structures are attractive for this purpose because their topology can be tailored to control mass distribution, load paths and local deformation modes[5-7]. Aluminium alloys further offer low density, processability and cost advantages[8-10]. In service environments such as aero-engine nacelles and thermal protection panels, however, aluminium lattice components can experience prolonged exposure to intermediate temperatures of approximately 200-400 °C[11]. Under these conditions, microstructural ageing in the alloy and the

macroscopic mechanical response of the lattice are coupled. Understanding this coupling is therefore essential for assessing service safety and avoiding premature failure in thermally loaded lightweight structures[12-14].

Several strategies have been developed to improve the high-temperature performance of aluminium alloys through compositional design and microstructural control. Conventional age-hardening 2xxx and 7xxx alloys rely on metastable Guinier-Preston zones or strengthening precipitates, which can dissolve or coarsen rapidly above 200 °C and cause a marked loss of strength[15-17]. By contrast, the rapid solidification associated with AM can produce supersaturated solid solutions, refined eutectic networks and metastable intermetallic compounds whose subsequent transformation can be exploited to improve thermal stability[18-20]. Hypereutectic Al-Si alloys use thermally stable Al-Si eutectic networks and primary Si particles for dispersion strengthening[21,22], whereas microalloying with Zr or Sc can form nanoscale precipitates that restrict recrystallisation and grain-boundary migration[23,24]. Transition elements such as Fe, Ni and Mn can also form stable intermetallic compounds, including Ni-, FeNi- and (Fe, Mn)-containing phases, that impede grain-boundary migration and dislocation motion at elevated temperature[25-27]. The Al-Si-Fe-Mn-Ni system is therefore of particular interest for SLM because Si improves melt fluidity and Fe-Mn-Ni additions promote high-temperature phase stability[28-30].

Maintaining mechanical stability during prolonged thermal exposure remains challenging because several irreversible microstructural processes occur simultaneously. Dispersoids can coarsen through Ostwald ripening, reducing Orowan strengthening[31]. For example, Jin *et al.*[32] reported that needle-shaped β-Mg2Si precipitates in an Al-13%Si alloy coarsened from 80-120 nm to approximately 2 μm after exposure at 300 °C for 1,000 h, accompanied by substantial property degradation. Other studies have shown that α-Al(Mn,Fe)Si dispersoids can coarsen and decrease in volume fraction during thermal exposure, reducing yield strength[33]. In parallel, metastable

phases can transform towards equilibrium phases, solutes can segregate to grain boundaries and coarse brittle phases can form at preferred crack-initiation sites[34]. Grain-boundary migration, subgrain coalescence and dislocation rearrangement further reduce the strengthening contribution of the initial microstructure[35,36]. Most available work has focused on bulk alloys or short-term heat treatments; comparatively little is known about how these ageing processes alter the failure behaviour of architected lattice structures during long-term exposure.

For lattice structures, thermal stability is not governed by the alloy alone. Topology determines load transfer, stress concentration, effective buckling length and failure morphology, whereas thermal exposure changes the strength, stiffness, ductility, precipitate distribution and grain structure of the constituent material[37,38]. These two effects can interact non-linearly: a topology that performs well in the initial state may become less favourable once the constituent material softens and the limiting event changes from fracture to instability. Previous studies on SLM AlSi10Mg lattices have shown that high-temperature treatments can dissolve initial cellular structures, coarsen Si particles and alter fracture behaviour[39]. However, the topology-dependent transition between fracture-controlled and buckling-controlled failure under long-term thermal exposure has not been resolved.

Here, we investigate this time-dependent design problem using SLM-fabricated heat-resistant Al-Si-Fe-Mn-Ni alloy lattices. As outlined in Figure 1 (a-d), the study tests whether prolonged exposure at 200-300 °C changes the failure criterion of two lattice topologies with the same relative density. Compression testing and finite element modelling were used to identify the topology-dependent mechanical response and failure mode transition, while fracture analysis, TEM and EBSD were used to link the macroscopic behaviour to solute segregation, second-phase evolution and texture retention. This approach establishes a structure-material mechanism for designing aluminium lattice components for long-term thermal service.

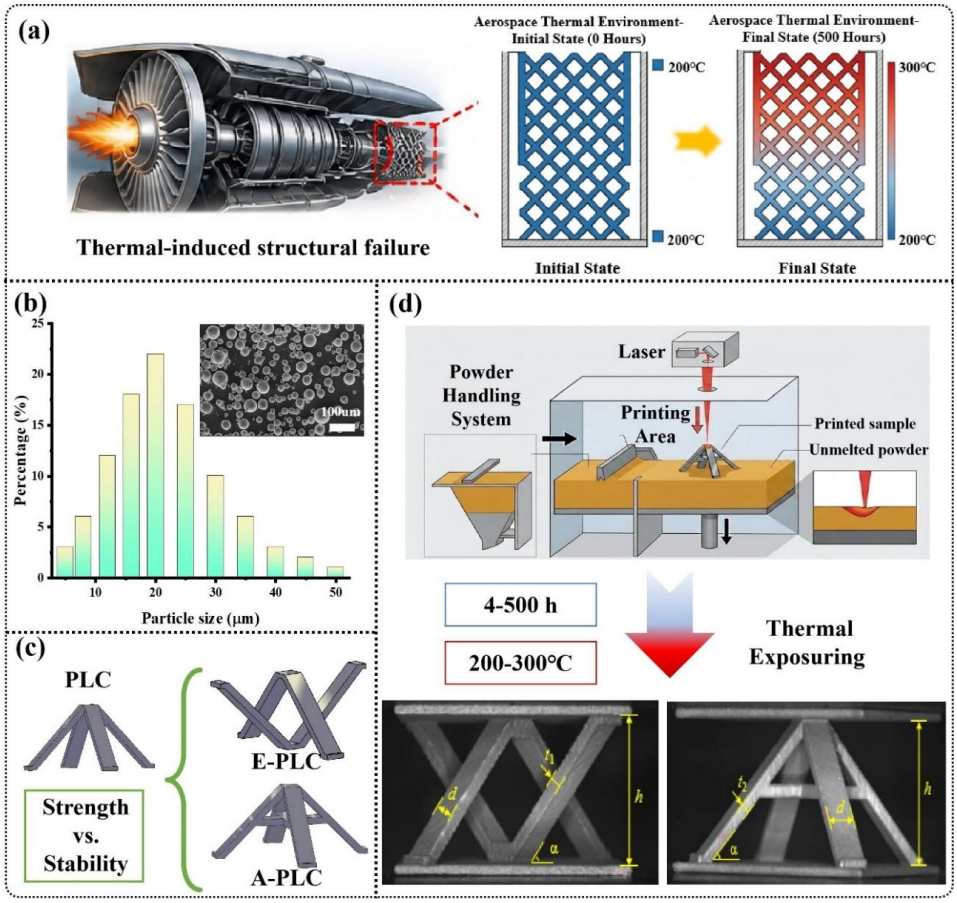

Figure 1. From powder to performance: (a) service environment and thermal loading; (b) feedstock powder characteristics; (c) topology design with strength-stability trade-off, and (d) additive manufacturing and thermal exposure governing failure evolution in lattice structures.

MATERIALS AND METHODS

Experimental materials and powder characteristics

Gas-atomized Al-Si-Fe-Mn-Ni heat-resistant aluminium alloy powder was used as the feedstock. The powder was mechanically sieved to obtain particles with a size range of 15-53 μm. Before SLM processing, the powder was vacuum dried at 75 °C for 6 h under a pressure of 1,000 Pa to remove adsorbed moisture and gases.

SLM fabrication process

The lattices were fabricated on a Farsoon FS273M system equipped with an IPG

YLS-500 continuous-wave fibre laser. Processing was conducted in a high-purity argon atmosphere with an oxygen content below 100 ppm, and the substrate was preheated to 140 °C. The optimized parameters were a laser power of 360 W, scanning speed of 1,400 mm s^{-1}, hatch spacing of 0.16 mm, layer thickness of 0.05 mm and laser spot diameter of approximately 100 μm. A scanning strategy with a 67° rotation between successive layers was used to reduce residual stress.

Lattice sandwich structures, tensile specimens and alloy blocks were fabricated using the same processing parameters. Two configurations based on the pyramid lattice cell were designed: an enhanced pyramid lattice cell with a central reinforcing rod (E-PLC) and an anti-symmetric pyramid lattice cell (A-PLC). The geometric parameters were h = 16 mm, d = 4 mm and α = 45°. To maintain the same relative density, the strut thicknesses of the E-PLC and A-PLC lattices were set to 1.15 mm and 1.50 mm, respectively. The tensile specimens followed ASTM E8/E8M[40,41], with a total length of 35 mm, a gauge length of 25 mm and a width of 6 mm. Alloy blocks with dimensions of 10 mm × 5 mm × 5 mm were prepared for microstructural characterization.

Thermal exposure treatment

To assess the effect of thermal exposure on mechanical properties and microstructure, lattice sandwich structures, tensile specimens and alloy blocks were subjected to isothermal treatment in a KSL-1， 200X box furnace. The exposure temperatures were 200 °C and 300 °C, and the holding times were 4, 20, 100 and 500 h. After exposure, all specimens were furnace-cooled to room temperature.

Mechanical properties testing

Compression tests on the lattice sandwich structures were performed using an INSTRON 5,985 universal testing machine under displacement control at 0.5 mm min^{-1}. Three specimens were tested for each condition, and the load-displacement response

was recorded throughout compression. Digital image correlation (DIC) was used to capture the deformation morphology during loading[42].

Tensile tests were performed on the same machine at a loading rate of 1.5 mm min^{-1} to determine the mechanical properties of the constituent alloy. Before testing, the specimen surfaces were sprayed with a black-and-white speckle pattern, and DIC was used to measure tensile strain. All tests were conducted at room temperature (25 ± 2 °C), with three specimens tested for each condition.

Material characterization

Scanning electron microscopy (SEM; Verios 5 UC, Thermo Fisher) was used to examine the fracture morphology of lattice struts. Electron backscatter diffraction (EBSD; Verios 5 UC, Thermo Fisher) was used to analyse grain morphology, local misorientation and crystallographic texture after thermal exposure. Samples for EBSD were ground, mechanically polished and then ion polished to improve indexing quality. Transmission electron microscopy (TEM) specimens were prepared by focused ion beam (FIB) milling and examined using a Talos F200X microscope operated at 200 kV. Scanning TEM high-angle annular dark-field (STEM-HAADF) imaging and energy-dispersive X-ray spectroscopy (EDS) were used to identify nanoscale phases and elemental segregation.

Finite element simulation

Finite element models of the two lattice configurations were established in Abaqus to analyse load-bearing behaviour and failure-mode evolution. The lattice geometries were meshed with a global element size of 0.3 mm based on mesh-convergence analysis, giving 126,755 elements for the E-PLC lattice and 99,040 elements for the A-PLC lattice. The bottom surface was fixed, and a displacement load was applied to the top surface through a coupled reference point. An elastoplastic constitutive model was defined using the tensile stress-strain curves measured under each thermal

exposure condition.

RESULTS

Performance degradation of lattice structures

Figure 2 shows the load-displacement curves and peak-load evolution of the two lattice structures after thermal exposure. Temperature and exposure time both affected the load-bearing response, but the effect was strongly temperature dependent. At 200 °C, neither topology showed an obvious reduction in peak load with increasing exposure time, indicating good structural stability under this condition. At 300 °C, by contrast, the elastic-stage slope decreased slightly and the peak load gradually declined with increasing holding time.

The degradation behaviour also depended on topology Figure 2(b-e). The A-PLC lattice exhibited an approximately logarithmic-linear decline in peak load with exposure time, whereas the E-PLC lattice degraded more rapidly during the early stage of exposure from 4 to 100 h. This contrast indicates that long-term high-temperature performance is controlled by both alloy stability and lattice topology, rather than by the heat resistance of the alloy alone.

Failure modes of lattice structures

Figure 2(f-g) compares the compressive failure morphologies of the two lattices after exposure at 300 °C. With increasing exposure time, the dominant failure mode shifted from brittle strut fracture to buckling instability. In the initial and short-exposure states, the E-PLC lattice mainly failed by brittle fracture near the junction between the cross core and inclined struts, accompanied by slight local buckling below the cross core. The A-PLC lattice showed a similar fracture-dominated response. After 500 h, the load-displacement curves decreased progressively after the peak without an abrupt load drop, and the compression images showed pronounced strut bending, particularly in the E-PLC lattice. These observations indicate that prolonged thermal exposure changes

the constituent material response and shifts the structural failure mode from early brittle fracture to progressive buckling.

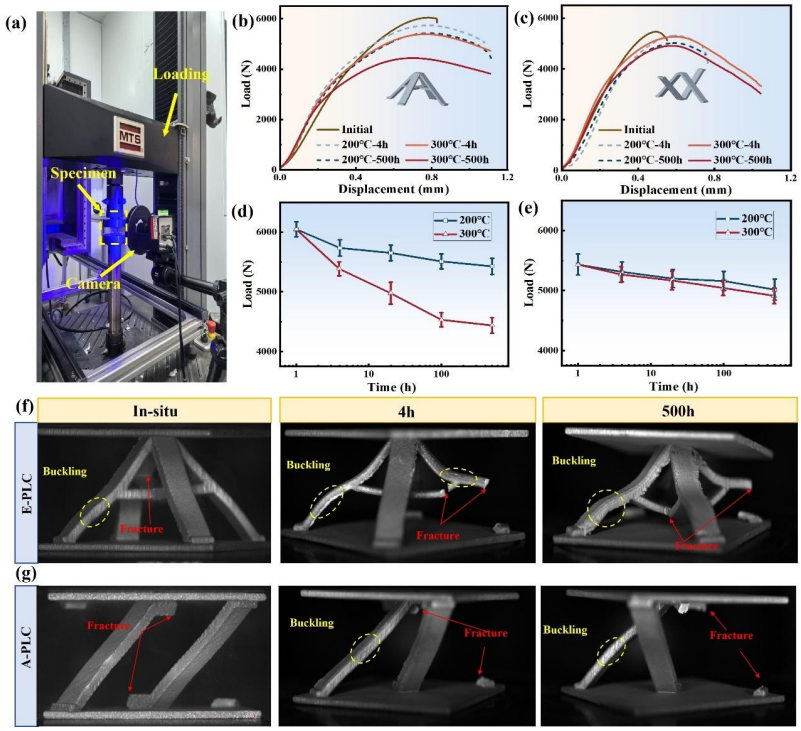

Figure 2. Compression failure characteristics of the two lattice structures under different thermal exposure durations: Load-displacement curves and performance degradation of two lattice structures under different thermal exposure conditions: (a) Test process; (b) Load-displacement curve of the E-PLC lattice; (c) Load-displacement curve of the A-PLC lattice; (d) Performance degradation of the E-PLC lattice; (e) Performance degradation of the A-PLC lattice; (f) *In-situ* evolution of failure modes of the E-PLC lattice (0 h, 4 h, and 500 h), showing the transition from fracture-dominated to buckling-assisted deformation; (g) *In-situ* evolution of failure modes of the A-PLC lattice (0 h, 4 h, and 500 h), highlighting the coupled fracture-buckling behavior under prolonged thermal exposure.

Effect of configuration

The above research indicates that the peak load degradation rate of the E-PLC lattice is higher than that of the A-PLC lattice with increasing thermal exposure time. To analyze

the underlying mechanism, according to Euler's formula[49], the pyramid lattice struts are primarily subjected to axial compressive loads, and its critical buckling load P_{cr} can be expressed as,

$$P_{cr}=\frac{\pi^2 EI}{(KL)^2} \quad (1)$$

where $\boldsymbol{E}$ is the elastic modulus of the material; $\boldsymbol{I}$ is the second moment of area; L is the length of the strut, and K is the effective length factor related to the boundary conditions. The formula reveals that a competitive mechanism exists between the *second moment of area effect* and the *cross-core support effect* in the two configurations:

- *Second moment of area effect*: At the same relative density, the E-PLC lattice has a smaller individual strut thickness (t_1=1.15 mm) compared to the A-PLC lattice (t_2=1.5 mm) due to the cross-core design. This results in a lower $\boldsymbol{I}$, theoretically making it more susceptible to buckling.

- *Cross-core support effect*: the cross-core design of the E-PLC lattice provides additional support constraints during the compressive process, effectively delaying the onset of buckling.

Given the inherent brittleness of the heat-resistant aluminum alloy at the initial state, the lattices undergo brittle fracture before buckling occurs. At this stage, the support offered by the cross core enables the E-PLC lattice to achieve a higher peak load than the A-PLC lattice. However, with prolonged thermal exposure, the lattice failure mode transitions from brittle fracture to buckling instability, implying that the material has not attained the ultimate strength when the lattice reached its peak load. Concurrently, the cross-core support effect on the E-PLC lattice diminishes due to the decline in the $\boldsymbol{E}$ of heat-resistant aluminum alloy. Consequently, the detrimental influence of the smaller

I for the E-PLC lattice became dominant, resulting in a significant reduction in the load-bearing capacity compared to the A-PLC lattice.

To verify this mechanism, tensile testing of the constituent alloy was combined with finite element modelling. Figure 3a shows that exposure at 300 °C progressively reduced strength and elastic modulus while increasing plastic strain. The alloy therefore underwent a brittle-to-ductile transition during thermal exposure, providing the material basis for the observed shift in lattice failure mode.

The finite element model used the experimentally measured elastoplastic constitutive response as input, and the predicted load-displacement curves are shown in Figure 3b. Because the model did not include damage evolution, it was not intended to reproduce abrupt fracture events. Instead, it was used to isolate how topology and stiffness changes influence buckling-controlled load-bearing behaviour.

The simulations show that, under the same exposure condition, the A-PLC lattice has higher stiffness than the E-PLC lattice because its thicker struts provide a larger second moment of area. The larger I also increases the critical buckling load. After localized plastic deformation begins, the lattice can continue to carry load without immediate collapse. In the initial state, the E-PLC cross core contributes to the post-yield load increase. After prolonged exposure, however, this reinforcing effect weakens as the constituent alloy softens, and the second-moment-of-area effect becomes more important. This change explains why the A-PLC topology exhibits better load-bearing retention after long-term thermal exposure.

The stress contours at peak load [Figure 3(c-d)] further support this interpretation. High stresses are concentrated at strut-panel junctions, on the inner side of bent struts and near cross-core regions, matching the experimentally observed fracture and buckling sites. The A-PLC lattice distributes bending into smaller and more symmetric

deformation modes, whereas the cross-core region in the E-PLC lattice introduces local stress concentration and asymmetric buckling. Because the peak stress levels of the two lattices are comparable, the difference in long-term load-bearing capacity is primarily attributed to topology-controlled instability resistance.

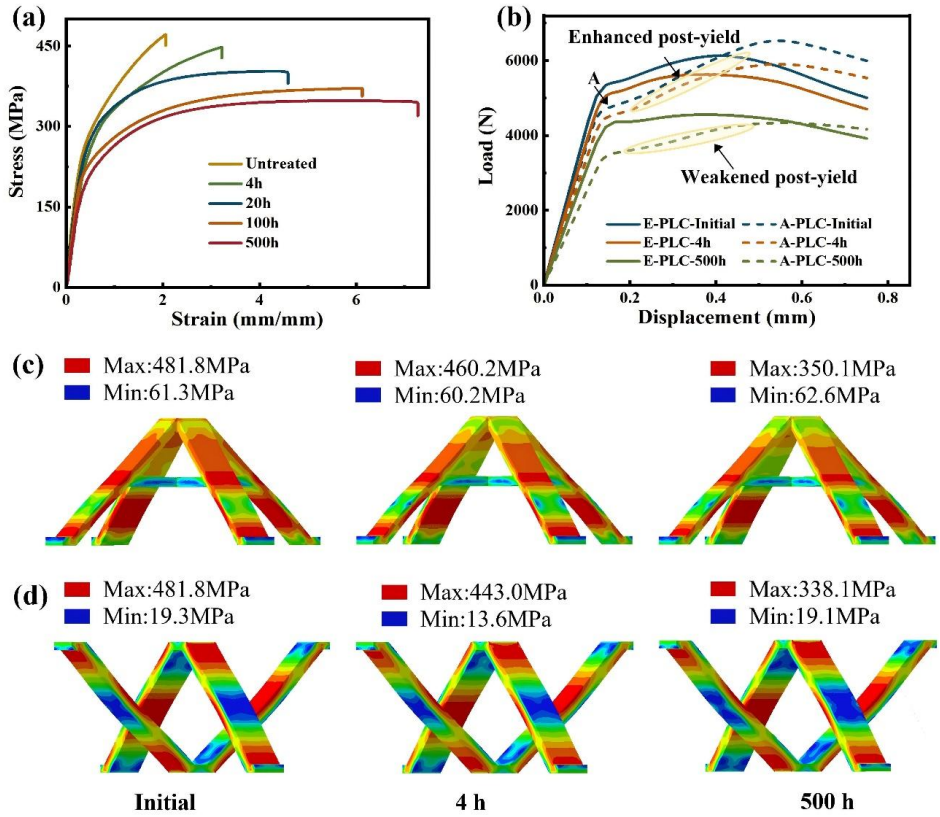

Figure 3. Tensile performance of heat-resistant aluminum alloy and FEM results of lattice structures under different thermal exposure durations: (a) Tensile stress-strain curve of heat-resistant aluminum alloy; (b) Load-displacement simulation curve of lattice structures; (c) Von Mises stress distribution in E-PLC lattice at peak load; (d) Von Mises stress distribution in A-PLC lattice at peak load.

MICROSTRUCTURAL EVOLUTION ANALYSIS

Fracture analysis

To systematically elucidate the microstructural origins of the macroscopic failure transition, Figure 4 presents a coupled qualitative and quantitative fractographic analysis of the lattice struts at 300 °C. The initial state exhibits a quasi-cleavage

topography characterized by localized micro-cracks and shallow, sub-micron dimples [Figure 4a] As thermal exposure proceeds to 4 h, thermodynamically driven elemental diffusion triggers the formation of new precipitates [Figure 4b]. These nanoscale obstacles effectively impede dislocation glide, amplifying the plastic strain energy dissipated during crack propagation. Consequently, the fracture morphology initiates a transition, reflected by the average dimple size expanding to 1.5 μm and the ductile fraction surging to 50%. Upon extended exposure to 500 h, the material undergoes a comprehensive brittle-to-ductile transition [Figure 4c]. This intrinsic brittleness is quantitatively corroborated by a constrained average dimple size of approximately 0.8 μm [Figure 4d] and a minimal ductile area fraction of only 20% [Figure 4e], seamlessly explaining the catastrophic structural fracture observed during initial compression. The sustained localized plastic flow around a denser precipitate network facilitates the development of large, deep dimples (ranging from 2 to 4 μm, averaging 3.2 μm), elevating the total ductile fraction to a dominant 85%. Ultimately, this progressive, quantitatively verified microstructural toughening serves as the fundamental material-level driving force that shifts the lattice's global failure mode from abrupt brittle fracture to progressive topological buckling.

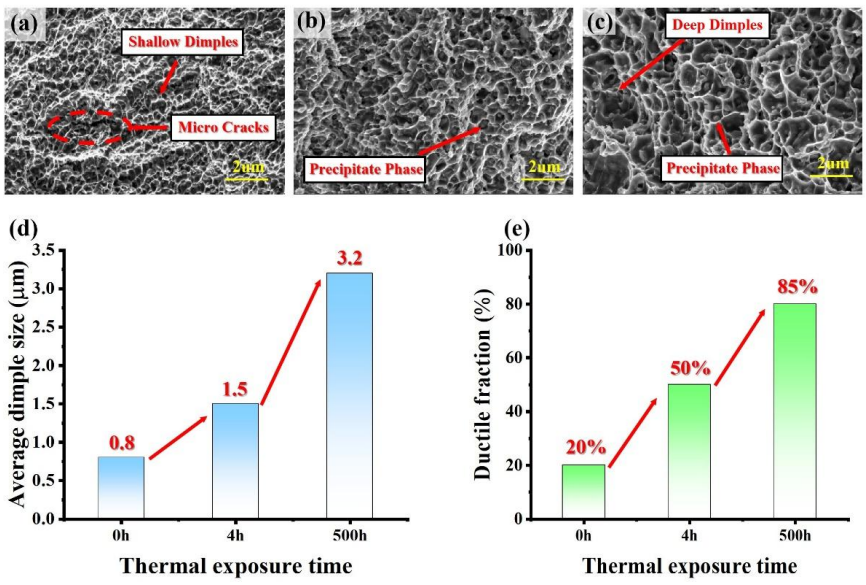

Figure 4. Precipitate-mediated fracture mode transition and quantitative dimple

evolution under high-temperature exposure at 300 °C: (a) Initial state showing shallow dimples and micro-cracks; (b) 4 h intermediate state showing larger dimples owing to the formation of new precipitates; (c) 500 h state featuring deep dimples typical of ductile fracture; and statistical increases in (d) average dimple size and (e) ductile area fraction over prolonged exposure durations.

Nanoscale precipitate evolution and solute segregation during thermal exposure

To elucidate the nanoscale phase transformations governing the macroscopic mechanical response, high-resolution electron microscopy was employed to track the microstructural evolution of the SLM-fabricated alloy during prolonged thermal exposure. Following an initial exposure at 300 °C for 4 h, the matrix exhibits a high-density, dual-scale dispersion of secondary phases [Figure 5a]. Quantitative imaging reveals that these nanoscale precipitates, ranging from 20 to 130 nm in diameter [Figure 5b], are uniformly distributed both intragranularly and along the grain boundaries. Detailed HRTEM coupled with EDS elemental mapping [Figure 5c-g] confirms significant local chemical partitioning. By explicitly correlating the elemental molar fractions [Figure 5h] with indexed lattice spacings and selected area electron diffraction patterns [Figure 5i-l], these early-stage precipitates are identified as complex hexagonal Al17(Fe3.2, Mn0.8)Si2, coexisting with metastable AlNi6Si3 and Al5(Fe, Ni) phases.

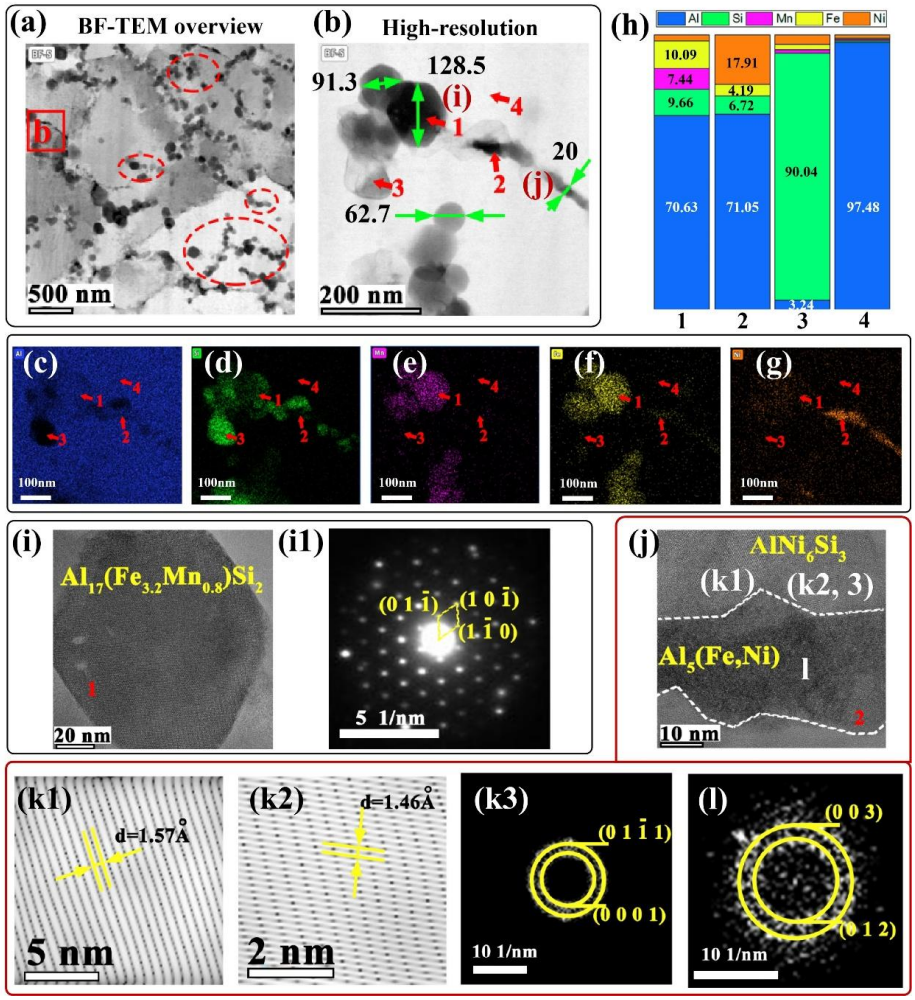

Figure 5. Microstructural characteristics of the SLM-fabricated heat-resistant aluminum alloy after thermal exposure at 300 °C for 4 h: (a) Bright-field TEM overview showing the distribution of precipitates; (b) magnified high-resolution image of a selected region detailing particle sizes; (c-g) EDS elemental mappings illustrating the local segregation of Al, Si, Mn, Fe, and Ni, respectively; (h) statistical elemental mole fractions at the denoted positions 1-4; (i) high-resolution TEM (HRTEM) image of position 1 with (i1) its corresponding selected area electron diffraction (SAED) pattern; (j) HRTEM image of the interface at position 2, accompanied by (k1-k2) measured lattice spacings and (k3, l) corresponding diffraction ring patterns for precise phase identification.

As the thermal exposure duration extends to 500 h, the alloy undergoes a microstructural transformation driven by long-range elemental diffusion [Figure 6]. The

initially dispersed second-phase particles experience substantial Ostwald ripening, coarsening to 80-180 nm, and transition into a highly localized, semi-continuous network along the grain boundaries [Figure 6(a-b)]. The corresponding energy dispersive spectroscopy (EDS) elemental mappings Figure 6(c-g), corresponding to Al, Si, Mn, Ni and Fe, respectively) directly visualize the elemental redistribution behavior: Al exhibits a uniform distribution in the aluminum matrix with a significant signal depression at the second-phase particles, while the alloying elements including Si, Mn, Fe and Ni are completely enriched in the second-phase particles, which are perfectly matched with the particle positions in the bright-field TEM images, and the marked positions 1-4 in the mappings are consistent with those in the high-resolution image. This spatial redistribution is accompanied by a purification of the aluminum matrix; EDS point analysis confirms that the intragranular Al concentration reaches an 98.68 at.% [Figure 6h, Point 1], signifying the near-complete depletion of dissolved alloying elements. Concurrently, localized nodes within this intergranular network exhibit extreme silicon enrichment (86.93 at.% at Point 2), indicating the *in-situ* precipitation of a nearly pure Si phase with negligible Al dissolution, alongside the complex transition-metal-rich intermetallics [Points 3 and 4] with co-enrichment of Mn, Fe and Ni, which is further validated by the consistent elemental distribution in the mappings.

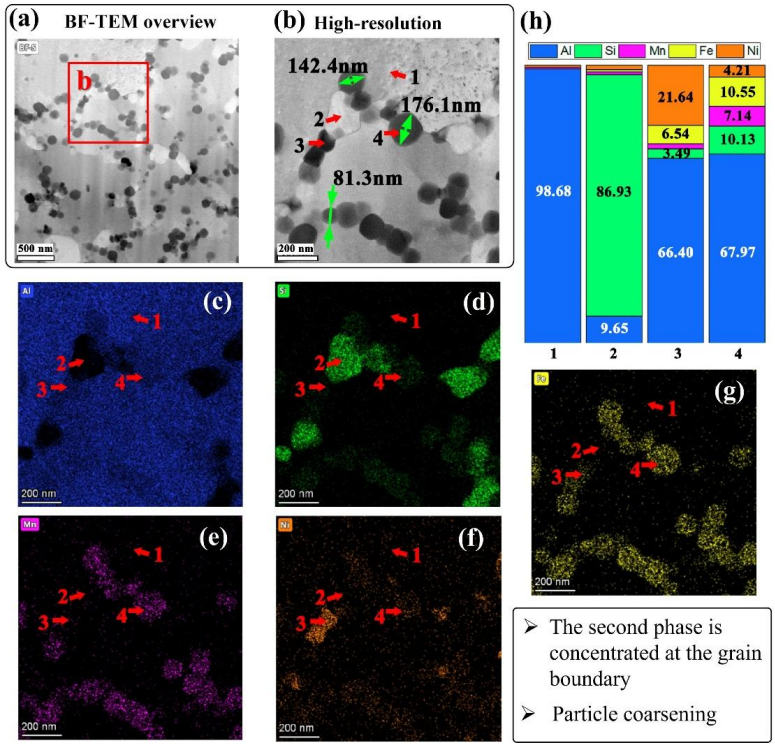

Figure 6. Thermodynamically driven solute segregation and grain-boundary precipitate network formation after prolonged thermal exposure at 300 °C for 500 h: (a) Bright-field TEM overview illustrating the intergranular concentration of coarsened precipitates; (b) magnified high-resolution view detailing particle sizes and selected analysis nodes; (c-g) EDS elemental mappings illustrating the distribution of Al, Si, Mn, Ni, and Fe, respectively; (h) quantitative elemental mole fractions at the denoted positions 1-4, confirming matrix purification and Si-rich phase precipitation.

To clarify the crystallographic nature of the grain-boundary network, the region from Figure 6a was further analyzed [Figure 7]. The microstructure features coarse intergranular precipitates and residual intragranular ultrafine dispersoids in the purified Al matrix [Figure 7a]. EDS mappings [Figure 7b-f] confirm strong intergranular segregation of Si, Mn, Fe and Ni, matching the precipitate positions. HRTEM of the Al matrix [Figure 7g] identifies a ~ 1° low-angle grain boundary, indicating minimal lattice distortion after long-term exposure. The precipitate-matrix interface is resolved in Figure 7h, with calibrated interplanar spacings matching the Al matrix and intermetallic phase. FFT indexing [Figure 7i1, j1] confirms the intergranular

precipitates at positions i and j are stable Al17(Fe3.2, Mn0.8)Si2 intermetallic. Discrete pure Ni [Figure 7k, k1] and pure Si [Figure 7l, l1] phases are also detected in the grain boundary network. This unique dual-scale architecture-a robust grain-boundary network coupled with resilient intragranular nanodispersoids-provides the fundamental crystallographic basis for the alloy's exceptional long-term thermal stability. The microstructural sequence detailed above reveals the fundamental phase transformation and stabilization mechanisms governing the alloy during prolonged thermal exposure. During the initial 4 h at 300 °C, thermal activation drives localized solute diffusion, triggering a dense and dispersive precipitation of metastable intermetallics both inside the grains and along their boundaries. With extended exposure, the thermodynamic drive to minimize interfacial energy forces solute atoms to segregate towards the grain boundaries via diffusion over extended distances. This ongoing elemental partitioning dictates two simultaneous processes: the Ostwald ripening of existing precipitates, and the progressive transition of metastable complex phases toward stable equilibrium states. Consequently, pure Ni and Si phases precipitate in situ, gradually assembling into a robust and nearly continuous network of secondary phases along the grain boundaries.

From a mechanical perspective, this intergranular network serves as a barrier, effectively pinning the boundaries via the Zener mechanism to suppress the coarsening and coalescence of the Al matrix at elevated temperatures. Concurrently, the residual ultrafine nanodispersoids strongly restrict dislocation glide via Orowan strengthening. It is this precise hierarchical architecture, comprising a resilient grain boundary network coupled with dense intragranular nanophases, that dynamically anchors the alloy microstructure and ensures its strength retention over extended thermal service.

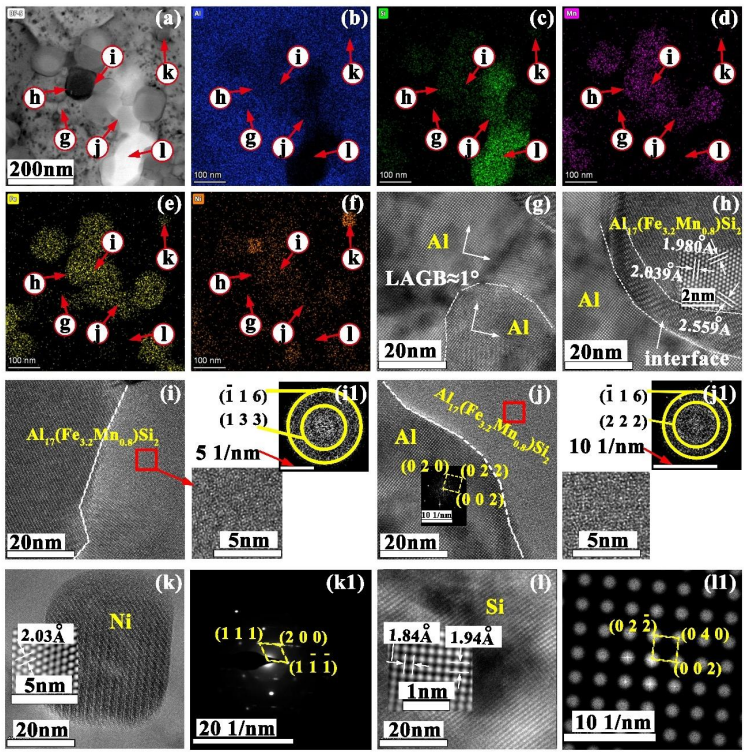

Figure 7. Microstructural and crystallographic characterization of the alloy after 500 h thermal exposure. (a) Bright-field TEM image of another typical grain boundary region of the sample after 500 h annealing; (b)-(f) Corresponding EDS elemental mappings showing the distribution of Al, Si, Mn, Fe, and Ni, respectively; (g)-(l) High-resolution TEM (HRTEM) images captured from the positions g, h, i, j, k and l marked in (a), respectively; (i1), (j1), (k1) and (l1) Corresponding fast Fourier transform (FFT) patterns of the selected regions in (i), (j), (k) and (l), respectively.

Mesoscale grain stabilization and texture retention during thermal exposure

To evaluate the mesoscale structural stability of the alloy, Figure 8 details the evolution of grain morphology and crystallographic texture using electron backscatter diffraction. The unindexed regions, appearing as white dots and representing the precipitated phases in the inverse pole figure maps [Figure 8(a1, b1)], display a dispersive distribution after 4 h but become heavily concentrated along the grain boundaries following 500 h of exposure. This visualizes the thermodynamically driven segregation of solute atoms toward the grain boundaries and the subsequent assembly of a continuous precipitate network. Concurrently, the elevated local misorientation within

the matrix, initially induced by the rapid solidification of the additive manufacturing process, is significantly alleviated after 500 h as shown in the kernel average misorientation maps [Figure 8(a2, b2)]. This reduction in local strain indicates that prolonged annealing provides ample activation energy for elemental diffusion, driving dissolved solutes toward a thermodynamically stable equilibrium state to fully precipitate.

Remarkably, despite this profound microstructural relaxation, statistical analysis [Figure 8(a4, b4)] reveals that the average grain size decreases slightly from 3.8 μm at 4 h to 3.2 μm at 500 h, alongside a notable increase in the fraction of grains smaller than 2.5 μm. This exceptional suppression of grain coarsening can be attributed to the robust Zener pinning effect exerted by the newly formed intergranular precipitate network, which firmly restricts the migration and coalescence of the aluminum matrix boundaries at elevated temperatures. Furthermore, the grain orientation spread maps [Figure 8(a3, b3)] demonstrate that the recrystallized fraction experiences only a marginal increase from 40.2% to 49.3%. Similarly, the pole figures [Figure 8(a5, b5)] confirm that the relative pole density and the initial crystallographic texture remain essentially unchanged. This combined stability in both grain architecture and crystallographic orientation confirms that the hierarchical distribution of the precipitate phases serves as the microscopic mechanism endowing the alloy with superior mechanical strength retention during extended thermal service.

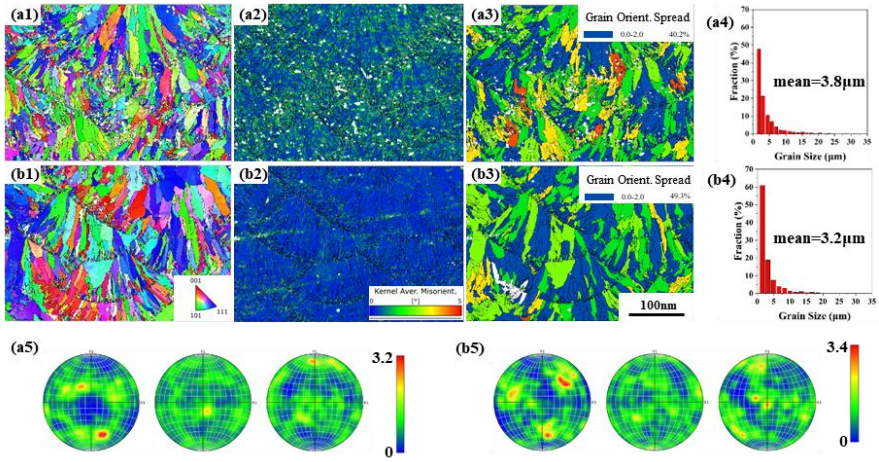

Figure 8. Electron backscatter diffraction characterizations of mesoscale grain stability and crystallographic texture retention of the alloy after thermal exposure at 300 °C. (a1-a5) Inverse pole figure map, kernel average misorientation map, grain orientation spread map, grain size distribution, and pole figures of the alloy after 4 h thermal exposure, respectively; (b1-b5) Corresponding EBSD analytical results of the alloy after 500 h thermal exposure.

CONCLUSION

This study examined the thermal stability of SLM-fabricated Al-Si-Fe-Mn-Ni alloy lattice structures by combining mechanical testing, finite element modelling and microstructural characterization. The main conclusions are as follows:

(1) The load-bearing response shows clear temperature dependence and topology dependence. Both lattices retained stable peak loads at 200 °C, whereas exposure at 300 °C caused gradual degradation with increasing holding time. The different degradation rates of the E-PLC and A-PLC lattices show that thermal stability is governed by the coupled effects of alloy ageing and lattice topology.

(2) Prolonged thermal exposure changes the governing failure criterion from brittle fracture to buckling instability. In the initial state, cross-core support allows the E-PLC lattice to reach a higher peak load. After long-term exposure, reduced stiffness and

increased ductility make buckling more decisive, and the larger second moment of area of the A-PLC struts provides better resistance to degradation.

(3) Solute atoms progressively segregate to grain boundaries during thermal exposure, forming a nearly continuous second-phase network. This network suppresses grain coarsening and helps retain the initial crystallographic texture through Zener pinning. Together with residual intragranular nanoparticles, this microstructure supports alloy-level thermal stability, while topology controls the lattice-level transition from fracture to buckling.

DECLARATIONS

Acknowledgments

We would like to thank all the collaborating institutions for their support in the completion of this manuscript.

Authors' contributions

Conceptualization, Methodology, Investigation, Data curation, Formal analysis, Writing-original draft, GM.Y;

Investigation, Validation, Formal analysis: DB.X;

Software, Visualization, Formal analysis: ZT.C;

Investigation, Resources: JM.F;

Validation, Visualization: SN.X;

Conceptualization, Funding acquisition, Project administration, Supervision, Writing-review and editing: HY.H;

Conceptualization, Supervision, Writing-review and editing: B.J.

Availability of data and materials

Not applicable.

AI and AI-assisted Tools Statement

Not applicable.

Financial support and sponsorship

This work was primarily supported by the Jihua Laboratory Internal Research Program (Grant No. X241941TB24R) and the National Natural Science Foundation of China (Grant No. 52304398), together with the National Natural Science Foundation of China (Grant Nos. 12141203 and 82272155), the Fundamental Research Funds for the Central Universities (Grant No. D5000230052), the Shaanxi Innovation Ability Support Plan Project Funds (Grant No. 2024RS-CXTD-29), the Northwestern Polytechnical University Doctoral Dissertation Innovation Foundation (Grant No. CX2025100), the Practice and Innovation Funds for Graduate Students of Northwestern Polytechnical University (Grant No. PF2025024), the Young Elite Scientists Sponsorship Program by CAST [Ph.D. Fellowship Program: 156-O-430-0000867-9], the Key R&D Project in Shaanxi Province (Grant No. 2024GX-YBXM-263), and the Shaanxi Provincial Science and Technology Industry Innovation Center for “Aircraft Composite Material Structure Design and Application”.

Conflicts of interest

All authors declared that there are no conflicts of interest.

Consent for publication

Not applicable.

Copyright

© The Author(s) 2026.

REFERENCES

1. Song Y, Xu S, Sato S, et al. A lightweight shape-memory alloy with superior temperature-fluctuation resistance. *Nature.* 2025/02/01 2025;638(8052):965-71.[DOI: 10.1038/s41586-024-08583-7]

2. Chen J-J, Xie H, Liu L-Z, et al. Strengthening gold with dispersed nanovoids. *Science.* 2024;385(6709):629-33.[DOI: 10.1126/science.abo7579]

3. Yin B, Yong W, Zhu J, et al. Compositional design of Ni-based superalloys for

additive manufacturing: Progress and perspectives. Materials Science and Engineering: R: *Reports*. 2026/04/01/ 2026;169:101185.[DOI: 10.1016/j.mser.2026.101185]

4. Hou C, Yang G, Wan X, Chen J. Study of thermo-fluidic characteristics for geometric-anisotropy Kagome truss-cored lattice. *Chinese Journal of Aeronautics.* 2019/07/01/ 2019;32(7):1635-45.[DOI: 10.1016/j.cja.2019.03.023]

5. DebRoy T, Wei HL, Zuback JS, et al. Additive manufacturing of metallic components – Process, structure and properties. *Progress in Materials Science.* 2018/03/01/ 2018;92:112-224.[DOI: 10.1016/j.pmatsci.2017.10.001]

6. Saha SK, Wang D, Nguyen VH, Chang Y, Oakdale JS, Chen S-C. Scalable submicrometer additive manufacturing. *Science.* 2019/10/04 2019;366(6461):105-9.[DOI: 10.1126/science.aax8760]

7. Xiang S, Dong Z, Jia B, Chen B, Huang H. A new hybrid TPMS design with excellent thermo-mechanical performance. *International Journal of Mechanical Sciences.* 2026/01/15/ 2026;310:111132.[DOI: 10.1016/j.ijmecsci.2025.111132]

8. Shyam A, Bahl S. Heat-resistant aluminium alloys. *Nature Materials.* 2023/04/01 2023;22(4):425-6.[DOI: 10.1038/s41563-022-01436-6]

9. Sun W, Zhu Y, Marceau R, et al. Precipitation strengthening of aluminum alloys by room-temperature cyclic plasticity. *Science.* 2019/03/01 2019;363(6430):972-5.[DOI: 10.1126/science.aav7086]

10. Dong Z, Cheng W, He Y, Jia B, Wan X, Huang H. A Janus-Like Bio-Inspired Strategy for 3D-Printed Bimetallic Metamaterials with Excellent Thermal-Protection and Load Bearing Capacity. *Advanced Science.* 2026/04/01 2026;13(20):e24116.[DOI: 10.1002/advs.202524116]

11. Yan J, Gao Y, Xiang S, Zhan J, Jin L, Hua]ng H. A Strategy for 3D Printed Al-Based Bi-Material Lattice Optimization: Thermal-Mechanical Coupling Performance with Load-Bearing and Energy-Absorption. *Advanced Functional Materials.* 2026/03/01 2026;36(20):e21424.[DOI: 10.1002/adfm.202521424]

12. Ren X, Dai Y, Dong Z, Jia B, Zhao M, Huang H. Mechanical property and failure characteristic of CFRP composite bolted structure ranging from -55°C to 150°C. *Thin-Walled Structures.* 2025/12/01/ 2025;217:113787.[DOI: 10.1016/j.tws.2025.113787]

13. Wang F, An X, Wang Z, et al. Enhanced strength and ductility of high-entropy alloy via dislocation-mediated heterogeneous martensitic transformation. *Microstructures.*

2025;5(4):2025088.[DOI: 10.20517/microstructures.2025.33]

14. Liu Z, Tan Z, Zhou Z, et al. Hot isostatic pressing induced precipitation strengthening at room and high temperature of Ni-Fe-Cr-Al-V high-entropy alloy manufactured by laser powder bed fusion. *Microstructures*. 2024;4(2):2024024.[DOI: 10.20517/microstructures.2023.65]

15. Aboulkhair NT, Simonelli M, Parry L, Ashcroft I, Tuck C, Hague R. 3D printing of Aluminium alloys: Additive Manufacturing of Aluminium alloys using selective laser melting. *Progress in Materials Science.* 2019/12/01/ 2019;106:100578.[DOI: 10.1016/j.pmatsci.2019.100578]

16. Martin JH, Yahata BD, Hundley JM, Mayer JA, Schaedler TA, Pollock TM. 3D printing of high-strength aluminium alloys. *Nature.* 2017/09/01 2017;549(7672):365-9.[DOI: 10.1038/nature23894]

17. Zhou SY, Su Y, Wang H, Enz J, Ebel T, Yan M. Selective laser melting additive manufacturing of 7xxx series Al-Zn-Mg-Cu alloy: Cracking elimination by co-incorporation of Si and TiB2. *Additive Manufacturing.* 2020/12/01/ 2020;36:101458.[DOI: 10.1016/j.addma.2020.101458]

18. Zhu Y, Zhang K, Meng Z, et al. Ultrastrong nanotwinned titanium alloys through additive manufacturing. *Nature Materials*. 2022/11/01 2022;21(11):1258-62.[DOI: 10.1038/s41563-022-01359-2]

19. Peng J, Li J, Liu B, Fang Q, Liaw PK. Origin of thermal deformation induced crystallization and microstructure formation in additive manufactured FCC, BCC, HCP metals and its alloys. *International Journal of Plasticity.* 2024/01/01/ 2024;172:103831.[DOI: 10.1016/j.ijplas.2023.103831]

20. Lv J, Liang Y, Xu X, et al. Performance-control-orientated hybrid metal additive manufacturing technologies: state of the art, challenges, and future trends. *International Journal of Extreme Manufacturing.* 2024/04/02 2024;6(3):032009.[DOI: 10.1088/2631-7990/ad3315]

21. Yan J, Dong Z, Jia B, et al. Thermal-Mechanical Coupling Performance of Heat-Resistant, High-Strength and Printable Al-Si Alloy Antisymmetric Lattice Structure. *Advanced Science.* 2024/11/01 2024;11(42):2407107.[DOI: 10.1002/advs.202407107]

22. Dong Z, Jia B, Cheng W, et al. Heat resistant ultra-strong Al-Si alloy and its application in additive manufacturing. *Cell Reports Physical Science.* 2025;6(8) [DOI:

10.1016/j.xcrp.2025.102774]

23. Glerum JA, Kenel C, Sun T, Dunand DC. Synthesis of precipitation-strengthened Al-Sc, Al-Zr and Al-Sc-Zr alloys via selective laser melting of elemental powder blends. *Additive Manufacturing.* 2020/12/01/ 2020;36:101461.[DOI: 10.1016/j.addma.2020.101461]

24. Chen L, Yang J, Zhang Y, et al. Synthesis of Al–Zr master alloy in KF–AlF3–ZrO2 melts by aluminothermic reduction–molten salt electrolysis. *Journal of Cleaner Production.* 2022/12/10/ 2022;378:134579.[DOI: 10.1016/j.jclepro.2022.134579]

25. Deng J, Chen C, Liu X, Li Y, Zhou K, Guo S. A high-strength heat-resistant Al−5.7Ni eutectic alloy with spherical Al3Ni nano-particles by selective laser melting. *Scripta Materialia.* 2021/10/01/ 2021;203:114034.[DOI: 10.1016/j.scriptamat.2021.114034]

26. Wang Y, Freiberg D, Huo Y, et al. Shapes of nano Al6Mn precipitates in Mn-containing Al-alloys. *Acta Materialia.* 2023/05/01/ 2023;249:118819.[DOI: 10.1016/j.actamat.2023.118819]

27. Wan T, Huang Z, Cheng Z, et al. The effect of chromium content on the corrosion behavior of ultrafine-grained CrxMnFeCoNi high-entropy alloys in sulfuric acid solution. *Microstructures.* 2023;3(2):2023014.[DOI: 10.20517/microstructures.2022.36]

28. Cai Q, Lordan E, Wang S, et al. Die-cast multicomponent near-eutectic and hypoeutectic Al–Si–Ni–Fe–Mn alloys: Microstructures and mechanical properties. *Materials Science and Engineering: A.* 2023/05/08/ 2023;872:144977.[DOI: 10.1016/j.msea.2023.144977]

29. Cai Q, Fang C, Lordan E, Wang Y, Chang ITH, Cantor B. A novel Al-Si-Ni-Fe near-eutectic alloy for elevated temperature applications. *Scripta Materialia.* 2023/12/01/ 2023;237:115707.[DOI: 10.1016/j.scriptamat.2023.115707]

30. Rakhmonov JU, Vo NQ, Croteau JR, Dorn J, Dunand DC. Laser-melted Al-3.6Mn-2.0Fe-1.8Si-0.9Zr (wt%) alloy with outstanding creep resistance via formation of α-Al(FeMn)Si precipitates. *Additive Manufacturing.* 2022/12/01/ 2022;60:103285.[DOI: 10.1016/j.addma.2022.103285]

31. Zou Y, Cao L, Wu X, Mou C, Tang S. Revealing the coarsening behavior of precipitates and its effect on the thermal stability in T′ and η′ dual-phase strengthened Al-Zn-Mg-Cu alloys. *Journal of Materials Science & Technology.* 2025/06/10/

2025;220:54-66.[DOI: 10.1016/j.jmst.2024.09.010]

32. Jin L, Liu K, Chen XG. Improved Elevated Temperature Properties in Al-13%Si Piston Alloys by Mo Addition. *Journal of Materials Engineering and Performance.* 2020/01/01 2020;29(1):126-34.[DOI: 10.1007/s11665-019-04543-9]

33. Liu K, Ma H, Chen XG. Enhanced elevated-temperature properties via Mo addition in Al-Mn-Mg 3004 alloy. *Journal of Alloys and Compounds.* 2017/02/15/ 2017;694:354-65.[DOI: 10.1016/j.jallcom.2016.10.005]

34. Li Q, Wang J, Suleiman ZM, et al. AI assisted design of high thermal conductivity Al-Fe-Ni-Mg alloys. *Journal of Alloys and Compounds.* 2025/07/20/ 2025;1036:181839.[DOI: 10.1016/j.jallcom.2025.181839]

35. Xie J, Xiong Z, Zhang L, Zhao C. Dislocation engineering via Al3(Sc,Zr)-mediated coarse low-angle grain boundaries for breakthrough strength-ductility balance in Al-Zn-Mg alloys. *Materials & Design.* 2025/12/01/ 2025;260:115178.[DOI: 10.1016/j.matdes.2025.115178]

36. Zuo J, Hou L, Shi J, Cui H, Zhuang L, Zhang J. The mechanism of grain refinement and plasticity enhancement by an improved thermomechanical treatment of 7055 Al alloy. *Materials Science and Engineering: A.* 2017/08/15/ 2017;702:42-52.[DOI: 10.1016/j.msea.2017.06.106]

37. Wu M, Liu W, Xiao D, Huang L. Influence of thermal exposure on the microstructure evolution and mechanical behaviors of an Al-Cu-Li alloy. *Materials & Design.* 2023/03/01/ 2023;227:111767.[DOI: 10.1016/j.matdes.2023.111767]

38. Sun J, Liu J, Liu L, Zhou Y, Li J, Sun X. Effects of Al on microstructural stability and related stress-rupture properties of a third-generation single crystal superalloy. *Journal of Materials Science & Technology.* 2019/11/01/ 2019;35(11):2537-42.[DOI: 10.1016/j.jmst.2019.05.003]

39. Kuang J, Zhao X, Zhang Y, et al. Impact of thermal exposure on the microstructure and mechanical properties of a twin-roll cast Al-Mn-Fe-Si strip. *Journal of Materials Science & Technology.* 2022/04/30/ 2022;107:183-96.[DOI: 10.1016/j.jmst.2021.07.022]

40. Tradowsky U, White J, Ward RM, Read N, Reimers W, Attallah MM. Selective laser melting of AlSi10Mg: Influence of post-processing on the microstructural and tensile properties development. *Materials & Design.* 2016/09/05/ 2016;105:212-22.[DOI: 10.1016/j.matdes.2016.05.066]

41. Ren X, Dai Y, Dong Z, et al. Investigation on mechanical behavior and damage mechanism of T1000/BMI composite bolted joints under thermomechanical cycling of −80 °C~ 80 °C. *Composites Part B: Engineering.* 2026/02/15/ 2026;311:113261.[DOI: 10.1016/j.compositesb.2025.113261]

42. Li Y, Chen Z, Yang G, Han Z, Shen Q. The strain-rate-dependent tensile failure and energy-absorbing behavior of sheet molding compounds. *Composites and Advanced Materials.* 2024/08/01 2024;33:26349833241258497.[DOI: 10.1177/26349833241258497]